

Search for ambient superconductivity in the Lu-N-H system

Received: 21 April 2023

Accepted: 18 August 2023

Published online: 04 September 2023

 Check for updates

Pedro P. Ferreira^{1,2}, Lewis J. Conway^{3,4}, Alessio Cucciarì^{5,6},
Simone Di Cataldo^{5,7}, Federico Giannessi^{5,6}, Eva Kogler², Luiz T. F. Eleno¹,
Chris J. Pickard^{3,4} ✉, Christoph Heil² ✉ & Lilia Boeri^{5,6} ✉

Motivated by the recent report of room-temperature superconductivity at near-ambient pressure in N-doped lutetium hydride, we performed a comprehensive, detailed study of the phase diagram of the Lu–N–H system, looking for superconducting phases. We combined ab initio crystal structure prediction with ephemeral data-derived interatomic potentials to sample over 200,000 different structures. Out of the more than 150 structures predicted to be metastable within ~50 meV from the convex hull we identify 52 viable candidates for conventional superconductivity, for which we computed their superconducting properties from Density Functional Perturbation Theory. Although for some of these structures we do predict a finite superconducting T_c , none is even remotely compatible with room-temperature superconductivity as reported by Dasenbrock et al. Our work joins the broader community effort that has followed the report of near-ambient superconductivity, confirming beyond reasonable doubt that no conventional mechanism can explain the reported T_c in Lu–N–H.

The report of superconductivity (SC) at near-ambient conditions in N-doped lutetium hydrides¹ raised the hope that the century-old quest for room-temperature, ambient pressure SC was finally successful². A significant leap forward occurred when Mikhail Erements' group reported conventional SC with a T_c of 203 K in compressed sulfur hydride eight years ago³. The ensuing *hydride rush* led to the discovery of dozens of new superconductors with T_c 's exceeding 100 K in less than five years^{4–12}, thanks to an unprecedented synergy between theoretical ab initio methods and experimental investigations^{13,14}.

Unfortunately, the extreme pressures required to synthesize superhydrides (~Megabar) ultimately undermine the advantages of high- T_c for real-world applications. In the last two years, different routes have been proposed to reduce stabilization pressures, such as optimized chemical precompression and impurity doping in ternary hydrides^{15–19}.

The highest T_c predicted is comparable to the best predictions for non-hydride conventional superconductors ($T_c \lesssim 120$ K)^{20–24}. These values are sufficient for many applications that would benefit from cost-effective liquid nitrogen cooling, which requires temperature well below the *holy-grail* limit of room-temperature SC.

Theoretically, no fundamental argument prevents room-temperature SC at ambient pressure, even within the conventional electron–phonon (*el-ph*) pairing scenario. Superhydrides have, in fact, disproven the long-held Cohen–Anderson limit for SC, showing that there are materials whose *el-ph* coupling and phonon energies allow for SC at room temperature or even higher. Unfortunately, all examples known so far require Megabar synthesis pressure^{3,4,6,25–27}.

If the report of near-room temperature SC in Lu–N–H¹ is confirmed, this compound may be the first example of a still unknown class of conventional superconductors where exceptional *el-ph*

¹Universidade de São Paulo, Escola de Engenharia de Lorena, DEMAR, 12612-550 Lorena, Brazil. ²Institute of Theoretical and Computational Physics, Graz University of Technology, NAWI Graz, 8010 Graz, Austria. ³Department of Materials Science and Metallurgy, University of Cambridge, Cambridge CB30FS, UK. ⁴Advanced Institute for Materials Research, Tohoku University, Sendai 980-8577, Japan. ⁵Dipartimento di Fisica, Sapienza Università di Roma, 00185 Rome, Italy. ⁶Enrico Fermi Research Center, Via Panisperna 89 A, 00184 Rome, Italy. ⁷Institut für Festkörperphysik, Wien University of Technology, 1040 Wien, Austria. ✉ e-mail: cjp20@cam.ac.uk; christoph.heil@tugraz.at; lilia.boeri@uniroma1.it

coupling properties can be realized at near-ambient conditions, and this could initiate a *second* hydride rush.

The experimental information reported by ref.¹ is, however, insufficient to identify the exact chemical composition of the new “red matter” superconductor (as coined by the authors). The first attempts to reproduce the experimental results yielded compounds with similar X-ray and absorption spectra under pressure but no trace of SC^{28–35}. In this context, first-principles calculations represent an invaluable tool for investigating the possibility that a new phase with exceptional superconducting properties may exist in the Lu–N–H system.

This work aims to provide a thorough and accurate description of the near-ambient pressure superconducting phase diagram of the ternary Lu–N–H system, combining state-of-the-art, unconstrained structural searches and linear response calculations of the *el-ph* properties. Ultimately, our results will demonstrate that the Lu–N–H system lacks the conditions to harbor ambient SC within the conventional *el-ph* scenario.

Results and discussion

Lu–N–H phase diagram

The near-ambient superconducting state in Lu–N–H at 294 K and 1 GPa was characterized by ref.¹ through a variety of experimental techniques, including X-ray diffraction (XRD), energy-dispersive X-ray, Raman spectroscopy, as well as magnetic susceptibility, electrical resistance, and heat-capacity measurements. The onset of SC under compression is driven by a structural phase transition, associated with a change in the color of the sample from blue to pink. T_c is about 100 K at 1 GPa, where SC sets in, reaches a maximum of 300 K at 2 GPa, and drops to 200 K at 3 GPa, where another structural phase transition is observed, turning the color of the sample from pink to bright red. The XRD analysis revealed the presence of two different ternary, face-centered cubic (*fcc*) Lu-networks in nearly all samples. The main phase, compound A (as identified by the authors), was indexed to space group (SG) $Fm\bar{3}m$ with lattice constant $a = 5.033$ Å at ambient pressure and underwent a structural phase transition at 3 GPa to a lower-symmetric SG, $Immm$. The second phase (compound B) can also be indexed as $Fm\bar{3}m$, but with a substantially smaller lattice constant ($a = 4.7529$ Å).

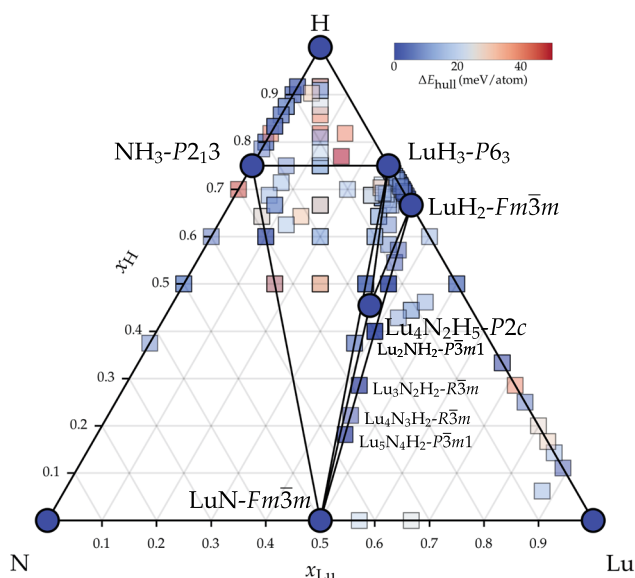


Fig. 1 | Phase diagram of the Lu–N–H ternary system at ambient pressure. Blue circles indicate the thermodynamically stable phases; metastable phases are shown as squares, colored according to their energy distance from the convex hull (ΔE_{hull}).

Besides these pieces of information, the authors do not report any further details: Due to the inability of conventional spectroscopy methods to accurately measure defect densities and fractional occupancies of light elements, such as hydrogen and nitrogen, even the chemical composition of the samples is unknown. Based on a comparison with known hydrides, the superconducting phase A was tentatively assigned to a $\text{LuH}_{3-\delta}\text{N}_\epsilon$ ternary structure, while compound B to rock-salt N-doped LuH. However, later theoretical and experimental works seem to suggest that phase A should most likely be characterized as pure or N-doped LuH_2 , which is compatible with both the XRD spectra and the reported color transition, but exhibits no SC^{28,29,33,34,36,37}. Furthermore, electronic structure calculations of the colors of hydrogen-defected cubic LuH_2 and LuH_3 show a strong dependence on hydrogen content, but no evidence for SC³⁸.

To identify structures likely to have formed in the experiments, we computed the ternary phase diagram at ambient pressure (0 GPa) and 10 GPa. To ensure that our structural search could find any relevant (meta)stable structure, we employed two different ab initio crystal structure prediction methods independently and in parallel, *viz.*, AIRSS (ab initio random structure search^{39,40}) employing ephemeral data-derived potentials (EDDPs)⁴¹, and evolutionary algorithms as implemented in USPEX^{42,43}. In total, we sampled over 200,000 structures. Afterward, the structures at each pressure were merged into a single database and relaxed with the same settings to obtain a single set of convex hulls – details in the Methods Section.

Figure 1 shows the calculated convex hull at 0 GPa. The convex hull obtained at 10 GPa is reported in Supplementary Fig. 4. Circles indicate thermodynamically stable phases which form the hull, while the squares indicate metastable phases up to 50 meV/atom above the hull, with the color of the symbols corresponding to the energy distance of each phase to the hull (ΔE_{hull}).

Focusing on the thermodynamically stable structures, the ternary Lu–N–H convex hull comprises four binary and one ternary phase. The binaries – $Fm\bar{3}m$ -LuN (NaCl prototype), $Fm\bar{3}m$ -LuH₂ (CaF₂ prototype), $P6_3$ -LuH₃, and $P2_1$ -NH₃ – have been experimentally reported before^{44,45} or are present in crystallographic databases^{46,47}. Our searches also reveal the ground state of LuH₃ to be of hexagonal symmetry, similar to the rhombohedral structure presented by ref. 36. As can be appreciated in the phonon dispersion plots (see below), however, this structure is dynamically unstable at the harmonic level. The cubic phase, $Fm\bar{3}m$ -LuH₃ (AlFe₃ prototype), is also dynamically unstable at ambient pressures within the harmonic approximation but was predicted to be stabilized at high pressures and to become superconducting with a T_c of 12.4 K (at 122 GPa)⁴⁸. Furthermore, some of the present authors have demonstrated recently that by including temperature and quantum anharmonic lattice effects, temperatures above 200 K can, in fact, stabilize the $Fm\bar{3}m$ -LuH₃ phase near ambient pressures⁴⁹. We provide the crystal structure information of all thermodynamically stable phases in Supplementary Tables 1 and 2.

$Fm\bar{3}m$ -LuN, $Fm\bar{3}m$ -LuH₂, and $Fm\bar{3}m$ -LuH₃ all contain *fcc* Lu lattices. $Fm\bar{3}m$ -LuN contains nitrogen atoms on the octahedral site and has a noticeably smaller lattice constant ($a = 4.76$ Å) than the two hydrides $Fm\bar{3}m$ -LuH₂ and $Fm\bar{3}m$ -LuH₃, where hydrogen occupies only tetrahedral and tetrahedral + octahedral sites, respectively ($a = -5.00$ Å).

The most stable structures all fall within the LuH₂–LuH₃–LuN tie-triangle. We identify a single ternary phase, $P2/c$ -Lu₄N₂H₅, as thermodynamically stable at 0 GPa. The crystal structure is shown in Fig. 2 and comprises layers of octahedral Lu–N bonds, as in $Fm\bar{3}m$ -LuN, and tetrahedral H–Lu bonds with interstitial H atoms in the octahedral site, similar to $Fm\bar{3}m$ -LuH₃, but with only half of the octahedral hydrogen sites occupied. This ternary phase, however, is only weakly metallic and is predicted to have a negligibly small T_c according to our calculations (see Table 1). A similar structure, with $C2/m$ symmetry, is only

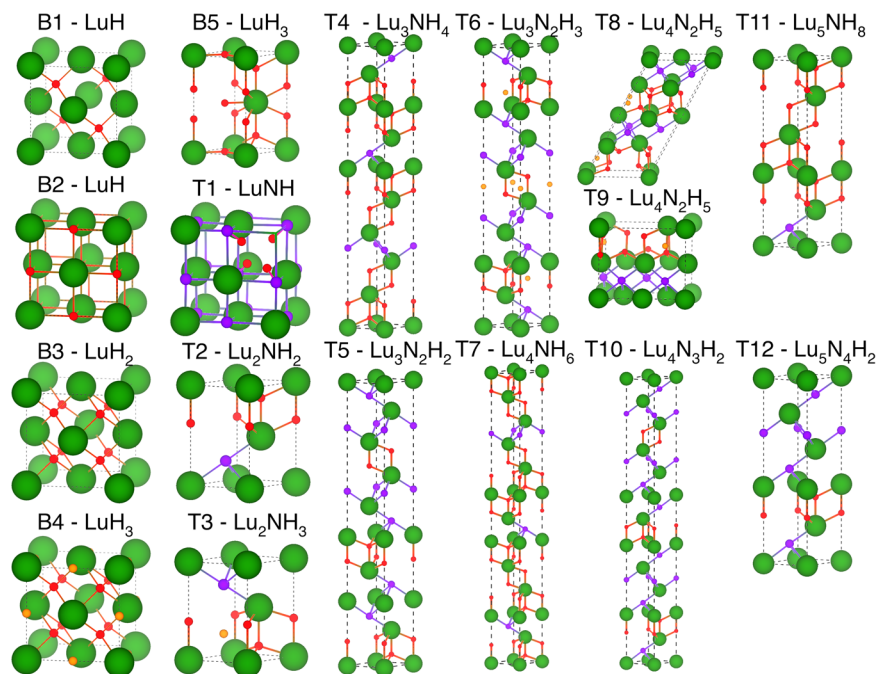


Fig. 2 | Crystal structures of the best candidates for SC in Lu–N–H ternary system as listed in Table 1. Lu, N, H, and H in octahedral sites are indicated as large green, medium purple, small red, and small orange spheres, respectively.

2 meV/atom higher in energy with an alternative distribution of occupied octahedral sites.

It should be noted at this point, nevertheless, that 7 ternary phases are less than 5 meV/atom distant from the hull, i.e., within the accuracy of electronic structure calculations. One also needs to consider that, depending on the system at hand and the particular synthesis route, metastable structures with enthalpies well above the convex hull can still be within reach of experimental synthesis⁵⁰. In fact, several of these ternary structures, which, as explained above, fall within LuH₂–LuH₃–LuN tie-triangle, are thermodynamically stable at 10 GPa. (see Supplementary Fig. 4).

Considering a reasonable range of 50 meV/atom for metastability, our calculations reveal over 160 structures, with about 100 being ternary compounds, which tend to cluster along the LuN–NH₃, LuN–LuH₃, LuN–LuH₂, NH₃–LuH₃, and LuN–H pseudo-binary lines. More than two-thirds (108) of the metastable (binary + ternary) structures are insulating. On the H-rich side, the typical structural pattern is characterized by H₂, NH, NH₂, and NH₃ molecules scattered around the Lu atom or embedded in disordered motifs of Lu–N–H substructures.

Of the 52 metallic structures, i.e., the only relevant ones for SC, 32 are binaries and 20 are ternaries. In Table 1 and Fig. 2, we collected the eleven ternary metallic structures which are also dynamically stable (T2–T12). All these structures fall within the LuH₂–LuH₃–LuN tie-triangle and are structurally very similar, comprising stacking-disordered *fcc* Lu with H and N on interstitial sites. The structures on the LuN–LuH₂ pseudo-binary line, i.e., *P* $\bar{3}$ *m*1–Lu₂NH₂, *R* $\bar{3}$ *m*–Lu₃NH₄, *R* $\bar{3}$ *m*–Lu₃N₂H₂, *R* $\bar{3}$ *m*–Lu₄N₃H₂, *P* $\bar{3}$ *m*1–Lu₅NH₈, and *P* $\bar{3}$ *m*1–Lu₅N₄H₂, all comprise layers of octahedral Lu–N bonds and tetrahedral Lu–H bonds.

The structures *R* $\bar{3}$ *m*–Lu₃N₂H₃ and *P* $\bar{3}$ *m*1–Lu₂NH₃ correspond to 2:1 and 1:1 mixtures of *Fm* $\bar{3}$ *m*–LuN and *Fm* $\bar{3}$ *m*–LuH₃, respectively. Hence, they appear as alternating layers – with different widths – of octahedral Lu–N bonds and H atoms on tetrahedral and fully occupied octahedral sites. These motifs are not particularly promising in terms of room temperature SC since in high-pressure superhydrides high-*T*_c SC usually occurs in phases with high H content in which H forms

covalent-metallic bonds either with another H (cage-like hydrides), or with a different element (covalent hydrides).

In addition to metastable, metallic ternary phases, Table 1 and Fig. 2 contain five binary phases (B1–*F* $\bar{4}$ 3*m*–LuH, B2–*Fm* $\bar{3}$ *m*–LuH, B3–*Fm* $\bar{3}$ *m*–LuH₂, B4–*Fm* $\bar{3}$ *m*–LuH₃, B5–*P*6₃/*mmc*–LuH₃), as well as one additional ternary phase (T1–*P*43*m*–LuNH). Except for B3–*Fm* $\bar{3}$ *m*–LuH₂, which is situated on the convex hull at 0 GPa, these phases are metastable but have been included nonetheless as they are compatible with the measured XRD spectra and/or have been suggested in other works as viable candidates to explain Dasenbrock-Gammon et al.’s experiments¹. Also these phases, which are structurally analogous to other low-pressure metal hydrides, such as Pd or Cr hydrides^{51,52}, are unlikely candidates for room-temperature SC.

Before discussing the superconducting properties in more detail, we briefly compare our calculated phase diagrams with the results of other independent crystal structure searches in the Lu–N–H system, which appeared in the literature during the preparation and revision process of our manuscript^{37,53–56}: ref. ⁵³ found six stable binary compounds and no stable ternaries at ambient pressure employing structural templates along with unified input parameters of the ATOMLY materials database. Interestingly, they report a thermodynamically stable *C2/c*–N₂H₃ phase, which does not show up in our dataset, even after performing fixed composition calculations on this stoichiometry. The phase diagrams reported by ref. ⁵⁴, ref. ³⁷, and ref. ⁵⁶, on the other hand, are consistent with ours, within an accuracy of 5 meV/atom. In particular, ref. ³⁷, who employed the open-source evolutionary algorithm XTALOPT⁵⁷, also identified the *P*43*m*–LuNH phase reported as T1 in Table 1, and also found it to be highly energetically metastable – i.e., 485 meV/atom (564 meV/atom) above the convex hull according to our (and their) calculations.

Mining for new superconductors in the Lu–N–H system

Table 1 summarizes the structural, thermodynamic, and superconducting properties of the structures identified as the most viable candidates for SC. The columns show the unique ID of the structure (B = binary / T = ternary) with a given composition and space group, the calculated distance from the hull (ΔE_{hull}), the logarithmic averaged

Table 1 | Summary of thermodynamic and superconducting properties for the metallic structures predicted at ambient pressure that may have been found in Dasenbrock-Gammon et al.'s experiment¹: (i) ternary phases within 50 meV/atom from the convex hull that are also dynamically stable and metallic and (ii) selected binary phases with LuH, LuH₂ and LuH₃ composition

ID	Comp.	SG	ΔE_{hull} (meV/atom)	ω_{log} (meV)	λ	η (10 ⁴ meV ²)	T_c^{AD} (K)	T_c^{E} (K)	XRD match	V_0 (Å ³ /n _{Lu})
B1	LuH	$F\bar{4}3m$	102	14.0	0.6	0.01	3.3	3.0	A	31.6
B2*	LuH	$Fm\bar{3}m$	222	24.4	0.9	0.05	17.2	18.6	B	27.6
B3	LuH ₂	$Fm\bar{3}m$	0	22.1	0.3	0.01	0.1	<0.5	A	31.6
B4*	LuH ₃	$Fm\bar{3}m$	101	17.6	1.7	0.05	25.4	32.0	A	31.3
B5*	LuH ₃	$P6_3/mmc$	10	21.5	1.7	0.08	31.9	38.5	none	34.7
B2 (5 GPa)	LuH	$Fm\bar{3}m$	–	24.3	0.7	0.04	9.8	9.7	–	–
T1	LuNH	$P\bar{4}3m$	485	18.5	1.0	0.03	15.6	16.0	A	31.1
T2	Lu ₂ NH ₂	$P\bar{3}m1$	5	27.3	0.3	0.02	0.0	<0.5	none	28.9
T3	Lu ₂ NH ₃	$P\bar{3}m1$	20	38.7	0.6	0.09	10.3	10.5	none	28.7
T4	Lu ₃ NH ₄	$R\bar{3}m$	6	26.2	0.3	0.02	0.1	<0.5	none	29.6
T5	Lu ₃ N ₂ H ₂	$R\bar{3}m$	2	27.2	0.2	0.02	0.0	<0.5	none	28.2
T6	Lu ₃ N ₂ H ₃	$R\bar{3}m$	14	40.7	0.5	0.08	4.4	4.9	none	28.0
T7	Lu ₄ NH ₆	$R\bar{3}m$	6	24.9	0.3	0.02	0.1	<0.5	none	30.1
T8	Lu ₄ N ₂ H ₅	$C2/m$	2	31.7	0.3	0.03	0.2	<0.5	none	28.7
T9	Lu ₄ N ₂ H ₅	$P2/c$	0	30.1	0.3	0.02	0.0	<0.5	none	28.7
T10	Lu ₄ N ₃ H ₂	$R\bar{3}m$	2	29.9	0.2	0.02	0.0	<0.5	none	27.9
T11	Lu ₅ NH ₈	$P\bar{3}m1$	6	24.9	0.3	0.02	0.1	<0.5	none	30.4
T12	Lu ₅ N ₄ H ₂	$P\bar{3}m1$	2	30.5	0.2	0.02	0.0	<0.5	none	27.6

Asterisks (*) indicate phases which, at the harmonic level, exhibit (few) harmonically-unstable modes, for which *el-ph* properties were computed integrating only on real (stable) modes. Phases with $T_c > 4$ K are discussed in greater detail. In the table, ΔE_{hull} is the energy distance of the compound from the calculated convex; ω_{log} is the logarithmic average phonon frequency; λ is the *el-ph* coupling strength; η is the McMillan-Hopfield parameter; and are the superconducting critical temperatures estimated from the semi-empirical Allen-Dynes formula and the isotropic Eliashberg equation, respectively; and V_0 is the unit cell volume per number of Lu atoms. Corresponding identifiers (ID), compositions (Comp.), space-group (SG), and XRD matches for the phases are provided.

frequency (ω_{log}), and the total *el-ph* coupling parameter (λ) computed from the Eliashberg functions, as well as the T_c estimated from the semi-empirical Allen-Dynes formula (T_c^{AD})⁵⁸ and the isotropic Eliashberg equation (T_c^{E}). In both cases, a standard value of $\mu^* = 0.1$ was assumed for the Morel-Anderson Coulomb pseudopotential. The meaning of the parameter η will be discussed in the following. The last two columns of the table indicate whether the calculated XRD pattern matches the experimental pattern reported in ref. 1 for the A (superconducting) or B (non-superconducting) phase, and the last column of the table lists the volume (V_0) per number of Lu atoms in the cell, which is a compact indicator of the number of octahedral/tetrahedral site occupation. Phases listed with an asterisk (*) are dynamically unstable at the harmonic level in some part of the Brillouin zone (BZ); the relative *el-ph* properties were obtained integrating over real frequencies.

Most phases listed in Table 1 have a negligibly small T_c i.e., are not superconducting. This is not surprising, considering that the (Lu+N):H ratio is low (≤ 3), limiting the possible contribution of hydrogen electronic and vibrational states to SC, and none of the structures examined contain metallic covalent H–H or H–N/Lu bonds.

The most promising ternary structures identified in our search have predicted T_c 's lower than 20 K: The $P\bar{4}3m$ -LuNH (T1) structure, with $T_c = 16.0$ K and $\Delta E_{\text{hull}} = 485$ meV/atom; $P\bar{3}m1$ -Lu₂NH₃ (T3), with $T_c = 10.5$ K and $\Delta E_{\text{hull}} = 20$ meV/atom; and $R\bar{3}m$ -Lu₃N₂H₃ (T6), with $T_c = 4.9$ K and $\Delta E_{\text{hull}} = 14$ meV/atom. A few binary phases, i.e., rocksalt B2- $Fm\bar{3}m$ -LuH, B4- $Fm\bar{3}m$ -LuH₃, and B5- $P6_3/mmc$ -LuH₃, with T_c 's of 18.6, 32.0, and 38.5 K, respectively, even outperform the ternaries.

Best superconducting candidates

In the following, we discuss the six phases indicated in Table 1 for which we calculated a non-negligible T_c . Figure 3 shows the corresponding phonon dispersions, (partial) phonon density of states (DOS), and isotropic Eliashberg functions $\alpha^2F(\omega)$.

B2-LuH. In our searches, the rocksalt Lu monohydride appears around 222 meV/atom above the convex hull. The H atoms occupy octahedral sites around Lu. With a volume of 27.6 Å³, this is one of the densest phases found in our search. In fact, the calculated XRD spectra match almost perfectly the XRD data for the non-superconducting B phase found in ref. 1 experiment. However, in pure B2- $Fm\bar{3}m$ -LuH, there should be no Raman-active modes, while ref. 1 Raman spectra exhibit several peaks around 100–250 cm⁻¹, probably due to structural distortions, and several peaks at very high frequencies (3000–4000 cm⁻¹), indicating trapped H₂ or N₂ molecules. At ambient pressure, RS-LuH is predicted to be dynamically unstable at the harmonic level – see Fig. 3a. Anharmonic effects are likely to harden the low-lying modes and remove the instability, as in rocksalt PdH⁵². A moderate pressure of 5 GPa has a similar effect, as can be appreciated in Fig. 3a.

Similarly to other low-pressure metal hydrides, the band structure of RS LuH derives from the hybridization of Lu-*d* and H-*s* states. Lu-*d* states fill the gap between H bonding-antibonding states, located at ± 7 eV around the Fermi level; the Fermi surface is dominated by Lu-*d* states, but the small residual H hybridization is sufficient to boost the T_c , providing a finite coupling with H modes. Integrating the Eliashberg function only on real frequencies yields $\omega_{\text{log}} = 24$ meV, $\lambda = 0.9$, providing a T_c of 18.6 K.

B4-LuH₃. $Fm\bar{3}m$ -LuH₃ is the structure originally proposed by ref. 1 for the high- T_c phase A, although later studies have suggested, instead, the non-superconducting B3- $Fm\bar{3}m$ -LuH₂ phase, which has the same *fcc* Lu sublattice and very close unit cell volume^{28,29,31–35}. $Fm\bar{3}m$ -LuH₃ appears about 100 meV/atom above the convex hull ($P6_3$ -LuH₃ turns out to be thermodynamically more stable). It crystallizes in the well-known DO₃ structure, in which the metal atoms form a face-centered-cubic lattice and hydrogen occupies all the tetrahedral and octahedral interstitial sites. Indeed, the simulated XRD spectrum agrees with the Bragg peaks of the A phase in ref. 1. However, the fully symmetric

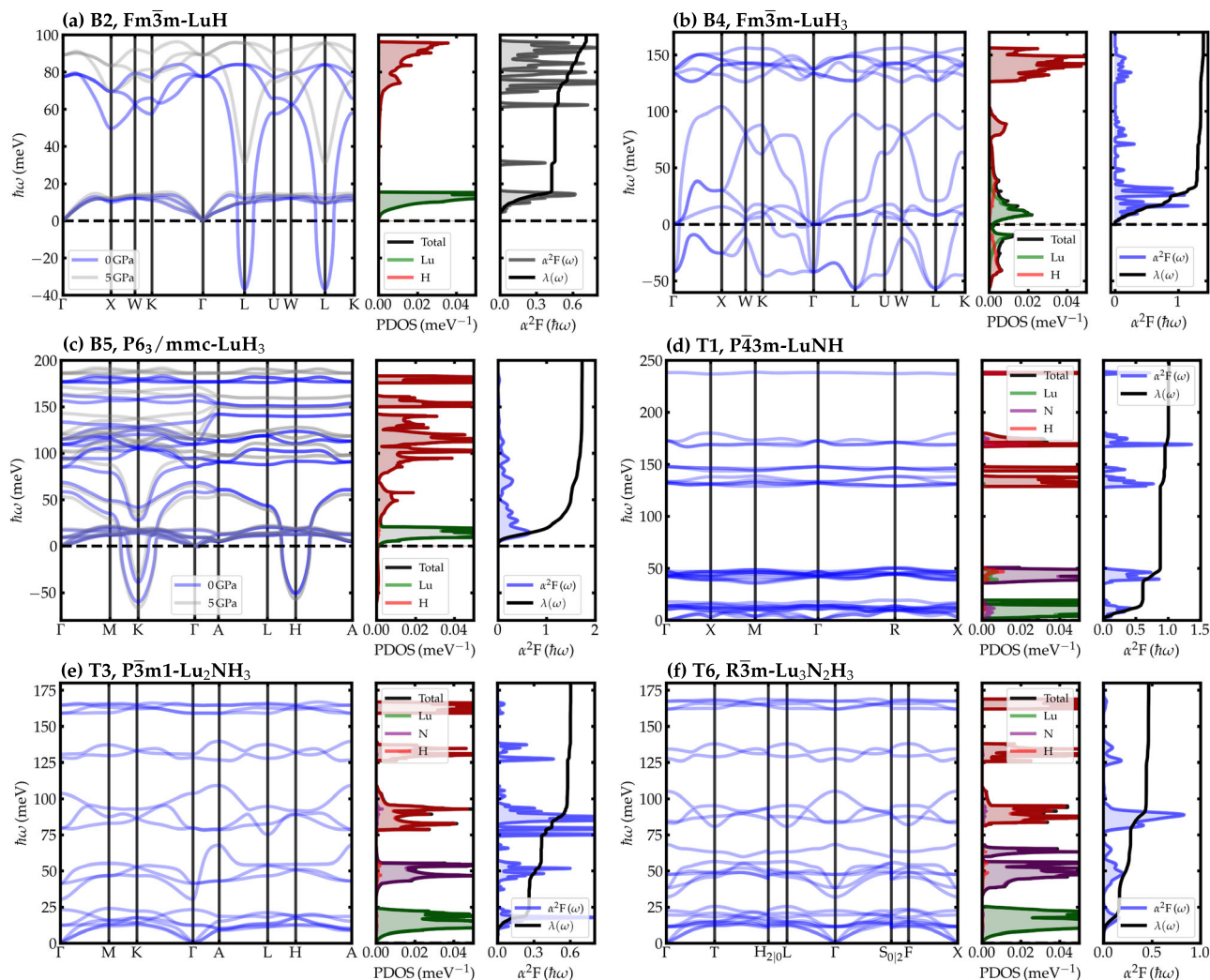


Fig. 3 | Phononic and superconducting properties of the best superconducting candidates. Phonon band structure (solid blue and light gray lines), phonon density of states (Lu PDOS in shaded green, N PDOS in shaded purple, and H PDOS in shaded red), isotropic Eliashberg function α^2F (shaded gray), and total $el-ph$

coupling parameter λ (solid black lines) for (a) B2, $Fm\bar{3}m$ -LuH, (b) B4, $Fm\bar{3}m$ -LuH₃, (c) B5, $P6_3/mmc$ -LuH₃, (d) T1, $P4_3m$ -LuNH, (e) T3, $P3m1$ -Lu₂NH₃, and (f) T6, $R\bar{3}m$ -Lu₃N₂H₃.

$Fm\bar{3}m$ phase should possess a single Raman active mode, for which we computed a frequency of 1079 cm^{-1} . Dasenbrock-Gammon et al.'s spectra comprise at least 11 peaks, with frequencies ranging from 100 to 1220 cm^{-1} .

As can be appreciated in Supplementary Fig. 9, the electronic structure comprises a metallic state with 3 bands crossing E_F . The Fermi level is right below a steep shoulder in the DOS, formed by unoccupied Lu- d bands, while occupied states are of mixed Lu-H character.

Our calculations show that at the harmonic level, several unstable modes exist in the entire BZ - Fig. 3b. Calculations by other authors show that the dynamic instability is not removed by moderate pressure and/or N substitution^{37,54}.

To obtain an estimate of T_c , we integrate the Eliashberg function only on real frequencies, obtaining $\lambda=1.65$ and $\omega_{\log}=17.6$ meV, resulting in $T_c=25.4$ K; the T_c obtained by solving the isotropic Eliashberg equations is higher ($T_c=32$ K), but still one order of magnitude too low for ambient SC.

Some of us have recently shown that $Fm\bar{3}m$ -LuH₃ could be stabilized by quantum anharmonic lattice effects at near ambient pressures for temperatures above 200 K⁴⁹. Increasing the pressure up to 6 GPa the temperature required for stability is reduced to $T>80$ K.

Still, the T_c for the quantum anharmonic- and temperature-stabilized $Fm\bar{3}m$ -LuH₃ phase is predicted to be between 50 and 60 K, i.e., well below RT, and in fact even well below the temperatures required to dynamically stabilize the structure⁴⁹.

B5-LuH₃. $P6_3/mmc$ -LuH₃ is only 10 meV/atom above the hull and assumes the Na₃As-prototype structure, which comprises two inequivalent Lu sites, with the first 4-coordinated to four equivalent H atoms and the second bonded in a trigonal planar geometry to three equivalent H atoms. As expected, the hexagonal symmetry does not produce any sizable match with the experimental XRD pattern of the A or B phases.

The Fermi level lies in a pseudogap formed by two-dimensional H- s hole-pockets around the zone center and Lu- d electron-pockets around the BZ corners, giving rise to a compensated (equal amounts of holes and electrons), low DOS at E_F .

As shown in Fig. 3c, the phonon dispersion reveals unstable modes around the K and H high-symmetry points in BZ, again indicative of lattice instabilities. We have checked that pressures up to 5 GPa cannot suppress the dynamic instability.

To estimate T_c , we again set the $el-ph$ matrix elements of all imaginary modes to zero. As a result, we get a high $el-ph$ coupling constant $\lambda=1.7$ and $\omega_{\log}=21.5$ meV, resulting in $T_c=31.9$ K (38.5 K) from

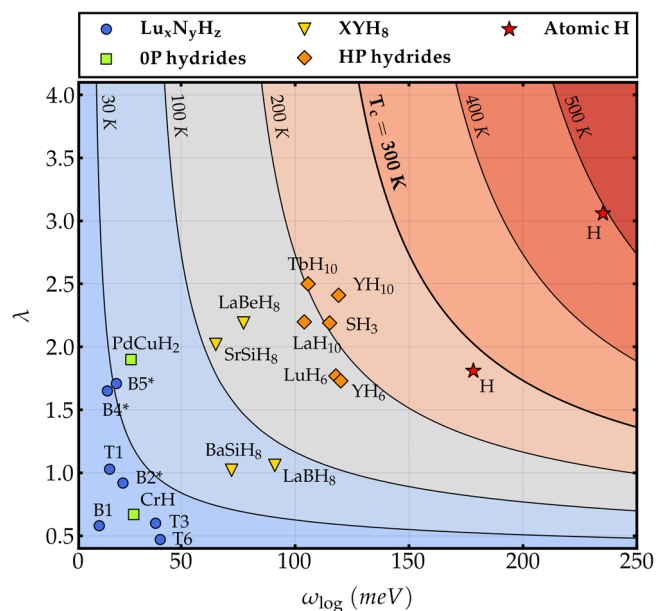


Fig. 4 | Electron-phonon coupling strength λ as a function of the logarithmic average phonon frequency ω_{\log} for different classes of superconducting hydrides. The best Lu-N-H hydrides considered in this work are indicated by blue circles and a selection of other hydrides is included as reference. Contour lines for T_c are plotted according to Eq. (1) with $\mu^* = 0.1$.

McMillan-Allen-Dynes formula (isotropic Eliashberg equations). Again, this value is too low to be compatible with room-temperature SC, even if the effects of anharmonicity or impurities are taken into account.

T1-LuNH. T1-LuNH is found 485 meV/atom above the convex hull in our search. It assumes a rocksalt structure with a *fcc* Lu-Lu sublattice with $a = 4.990 \text{ \AA}$, which matches considerably well the collected Bragg peak positions for the A phase (by comparing the simulated and measured XRD diffractograms, we obtain a normalized mean squared error of 0.17), representing 92.25% of the measured sample¹.

The structure is dynamically stable in the whole BZ at the harmonic level, but the calculated frequencies for the Raman-active modes do not match the main peaks of sample A reported in ref. 1, indicating again a strong effect of anharmonicities in the calculations and/or impurities or disorder in the measured samples.

LuNH is a multi-band metal with four bands crossing the Fermi level, which provide a high DOS at E_F of 2.57 states/eV. Most of these states, however, have Lu-*d* orbital character, representing 70% of the total DOS at E_F (see Supplementary Fig. 9); The H states only constitute 3.8% of the states around the Fermi level and thus do not considerably contribute to any *el-ph* coupling.

The total *el-ph* coupling $\lambda = 1.0$ is sizeable, but, as can be appreciated in Fig. 3d, originate mainly from low-frequency Lu and N vibrations. Hence, the corresponding ω_{\log} is very small (19 meV), and thus T_c is predicted to be about 16 K.

T3-Lu₂NH₃. Lu₂NH₃ is 20 meV/atom away from the convex hull at 0 GPa but is on the hull at 10 GPa, as shown in Supplementary Fig. 4. Its crystal structure resembles the well-known CdI₂ type, with one H atom being six-fold coordinated to Lu atoms to form edge-sharing LuH₆ octahedra. Nitrogen is intercalated between the lutetium layers, and the two additional H atoms are situated at the 2*d* Wyckoff position interstices between adjacent LuH₆ octahedra.

We find that the simulated XRD patterns match neither of the two patterns reported by ref. 1.

Interestingly, as shown in Supplementary Fig. 9, the electronic structure of Lu₂NH₃ shares some similarities with transition metal dichalcogenides⁵⁹ and MgB₂⁶⁰. The Fermi surface topology resembles

that of the prototypical charge-density-wave superconductors TiSe₂⁶¹, and ZrTe₂⁶². Two bands are crossing the Fermi level: a hole-like band crosses E_F around the Γ -A high-symmetry line, giving rise to out-of-plane quasi-cylindrical pockets derived from H-*s* orbitals, whereas an electron-like band derived from the Lu-*d* manifold crosses the Fermi level around the *L* direction in BZ. The strongly nested Fermi surface causes a largely anisotropic distribution of the *el-ph* coupling.

As can be appreciated in Fig. 3e, the vibrational frequencies extend up to 175 meV, and most of the *el-ph* coupling originates from the H-dominated phonon modes with energies between 75 and 110 meV. However, both the N-dominated modes (30–55 meV) as well as the Lu-dominated modes (below 25 meV) also contribute to λ . In contrast, the high-frequency vibrations of H (above 110 meV) give no significant *el-ph* contribution. In the end, we find $\lambda = 0.5$ and $\omega_{\log} = 41 \text{ meV}$, resulting in a $T_c = 5 \text{ K}$.

From the electronic dispersions and the momentum distribution of electron-phonon interactions of Lu₃NH₃, and their similarities with ZrTe₂, TiSe₂, and MgB₂, one can derive some intriguing conclusions that indicate that Lu₃NH₃, if stabilized, could be a promising platform to observe several exotic effects. First, the disconnected two-band Fermi surface with strongly distinct orbital projections could give rise to a two-gap superconducting state, which could significantly enhance the T_c ⁶³. Multi-gap SC may also give rise to an unusual response of the superconducting state to magnetic fields^{64,65}. Second, the low $N(E_F)$ of 0.25 states/eV and compensated electronic character, with nearly equal electron- and hole-type carriers at the Fermi surface, can cause the formation of electron-hole bound states⁶⁶, suggesting that excitonic contributions could be crucial in this system. Finally, the presence of hole-type H-*s* cylinders at the center of BZ leaves room for optimizing the T_c by increasing the hole pocket size through charge or chemical doping and strain engineering.

T6-Lu₃N₂H₃. $R\bar{3}m$ -Lu₃N₂H₃, which is only 14 meV/atom away from the convex hull, has the trigonal crystal structure of delafossite with H atoms in tetrahedral and octahedral sites, as schematically shown in Fig. 2. Again, we find no match with the experimental XRD patterns. Similarly to the previously discussed $P\bar{3}m1$ -Lu₂NH₃, the Fermi level is almost at the bottom of a pseudogap, resulting in a relatively low $N(E_F)$.

The largest contributions to λ originate from low-frequency Lu vibrations and the lowest branch of H vibrations (75–100 meV), as indicated in Fig. 3f. Thus, both λ and ω_{\log} are comparatively low (0.5 and 41 meV, respectively), resulting in a T_c of about 5 K.

How likely is conventional room-temperature superconductivity in Lu-N-H?

None of the metallic phases identified through our high-throughput screening of the Lu-N-H ternary hull at ambient pressure is compatible with the report of room-temperature SC by ref. 1. Indeed, the calculated T_c 's are below those predicted for many ambient-pressure metal hydrides and well below those anticipated for ternary sodalite-clathrate structures of La-B/Be or Ba/Sr-Si hydrides ($T_c \lesssim 120 \text{ K}$), which, according to calculations and recent experiments, may be quenched to near-ambient pressure^{16–18,67,68}.

Figure 4 compares the *el-ph* properties of our best Lu-H-N superconductors (blue circles) with those of other families of H-based superconductors, i.e., metal hydrides at ambient pressure (green squares), ternary XYH₈ sodalite-clathrate hydrides (yellow triangles), high-pressure binary hydrides (orange diamonds), and metallic hydrogen (red stars), on a ω_{\log} - λ diagram. The isocontours and color scale are obtained using the McMillan-Allen-Dynes formula⁵⁸ with $\mu^* = 0.1$:

$$k_B T_c^{\text{AD}} = \frac{\omega_{\log}}{1.2} \exp \left[-\frac{1.04(1+\lambda)}{\lambda(1-0.62\mu^*)-\mu^*} \right]. \quad (1)$$

Data were collected from refs.^{5,13,18,51,67,69–73} – additional details can be found in Supplementary Information.

Compounds belonging to different families cluster around different T_c isolines in ascending synthesis pressure. The increase in T_c seems to be solely driven by an increase of the logarithmically-averaged phonon frequency ω_{\log} , which varies from ~30 meV in ambient-pressure metal hydrides to 230 meV in atomic hydrogen at 2 TPa. ω_{\log} essentially measures the average stiffness of the phonon modes involved in the superconducting pairing.

A second material-dependent parameter, η , can be introduced to quantify the intensity with which these modes couple to electrons. η is related to the total *el-ph* coupling λ through the McMillan-Hopfield's formula $\lambda = \eta/\omega^{2,74}$, where ω is an average phonon frequency.

We have computed the values of η for all compounds in Fig. 4. Values of η range from $\eta = 10^2$ meV² in Lu–N–H and other low-P binary hydrides, to 10^4 meV² in binary and ternary sodalite-clathrate hydrides, and up to 10^5 meV² in atomic hydrogen – details in Supplementary Information. Differences in η typically reflect differences in chemical bonding, with larger values indicating more localized, directional bonds^{13,75}.

Our analysis leads us to two main conclusions regarding Dasenbrock-Gammon et al. data:¹ (i) All superconducting Lu–N–H phases identified in this work are essentially homogeneous and closely related to other low-pressure metal hydrides: SC is dominated by the metal sublattice, and hydrogen only plays a minor role, providing a marginal boost to the metal's T_c ¹³. Given that both ω_{\log} and η are one to two orders of magnitude too low for room-temperature SC, it is implausible that any renormalization effects due to distortions, impurities, or phonon anharmonicities may be invoked to explain Dasenbrock-Gammon et al. data¹; (ii) The only possibility to explain room-temperature SC is to hypothesize that an exotic phase has been realized in experiments where an extremely large *el-ph* coupling is concentrated in a small fraction of high-frequency modes ($\omega_{\log} > 150$ meV), like those provided by localized H–H or N–H vibrations. In fact, despite the dense hydrogen sublattice, even cage-like ternary sodalite clathrate hydrides cannot support T_c 's higher than 120 K at ambient pressure due to too low ω_{\log} and η . A preliminary scan of ternary structures in a reasonable metastability range can rule out this possibility.

Two recent works that appeared during the revision of our work^{76,77} seem to suggest that the inclusion of strong correlation effects in the Lu–N–H system by the so-called LDA+U method⁷⁸ may strongly affect our conclusions since the addition of a finite U on Lu leads to a rearrangement of the electronic structure, which in some particular structural models can sensibly boost the value of the DOS at the Fermi level.

However, it is well known that: (i) the relative band positions in the LDA+U approximation depend sensibly on the chosen value of U; (ii) values of U computed even in the most accurate constrained-random-phase approximation for the same compound may fluctuate depending on the details of the projection/downfolding procedure⁷⁹; in fact, ref. 80 have shown, by hybrid functional calculations, that different phases require different Hubbard potentials to describe the *f* electrons correctly. Even more crucial for the conclusions of the present work, however, is the fact that: (iii) including finite-bandwidth corrections in the Eliashberg theory for conventional SC washes out the effect of sharp peaks in the DOS^{81,82} and (iv) as shown in Fig. 4, even tripling the *el-ph* coupling constant of any of the predicted Lu–N–H phases would not be sufficient to bring the system even close to room-temperature SC without a simultaneous increase of the phonon frequency by an order of magnitude.

In summary, we have investigated the phase diagram and SC of the Lu–N–H system using state-of-the-art methods for crystal structure prediction.

The phase diagram of the Lu–N–H system is essentially determined by the thermodynamically stable binary phases $Fm\bar{3}m$ -LuN and $Fm\bar{3}m$ -LuH₂, and, to a lesser extent, $P2_13$ -NH₃. As a result, the ternary phases closest to the hull can be described as layered mixtures of the *fcc* LuN and LuH₂ phases or as H atoms trapped in an *fcc* LuN lattice. Some of these phases do match the XRD patterns reported by ref. 1, suggesting that the diffusion of N or H into a rock-salt LuN sublattice, which is justified from a thermodynamical point of view, may explain the formation of ternary phases in experiments. We note, however, that none of the stoichiometrically pure phases described here matches the reported Raman spectra, indicating a likely presence of impurities or distortions in the experimental samples.

A direct calculation of the superconducting properties of all metastable predicts no superconductor with a T_c higher than 40 K, almost an order of magnitude less than the result of ref. 1. Indeed, electronic structure calculations do not support high- T_c conventional SC in any of the examined structures.

Our results demonstrate unambiguously that Lu-hydrides, whether doped with N or not, cannot harbor ambient SC within the *el-ph* mechanism. The high fraction of Lu-*d* states at the Fermi level, the weak coupling between the already scarce low-energy H-*s* states with the high-frequency optical modes, and the substantially low ω_{\log} make the Lu–H–N system highly unlikely to meet the extraordinary conditions required for ambient SC.

While we acknowledge that strong electronic correlations may have a quantitative impact on the electronic properties of some of the calculated phases, the discrepancy between our calculated phonon frequencies and electron–phonon matrix elements and the measured T_c is too large to be explained by any renormalization effect on the electronic DOS^{76,77}. Therefore, we maintain that unless experiments unambiguously demonstrate the synthesis of such an exotic phase, the century-old *Sisyphus*' quest of ambient SC still remains open.

Methods

Crystal structure predictions

Crystal structure predictions were carried out using two different methods: (i) evolutionary algorithms as implemented in the USPEX package^{42,43} and (ii) ab initio random structure searching (AIRSS)^{39,40}. The structures resulting from the two runs were then relaxed using the same numerical parameters and merged into a single convex hull. In the following, we summarize the technical details of the USPEX search, the AIRSS search, and the final relaxation. Further computational details are provided in Supplementary Methods.

USPEX. We performed two sets of ternary and binary variable-composition searches at 0 and 10 GPa employing cells with 8–16 and 12–24 atoms. Pseudo-binary searches were also conducted along the selected lines corresponding to all possible two-phase reactions between the known stable binaries. Additionally, we also performed fixed-composition structural searches along the LuNH_x ($x = 1, 2, \dots, 23$) stoichiometries. Each structure was fully relaxed using VASP⁸³ employing a 5-step relaxation procedure. In total, more than 100,000 structures were sampled in our USPEX searches.

AIRSS. We used AIRSS accelerated by ephemeral data-derived potentials⁴¹ (EDDPs, the details of which are presented in the Supplementary Information) to search for structures in the Lu–N–H and LuH₂–LuN–LuH₃ ternary and pseudo-binary systems at 0, 2 and 10 GPa. Approximately 100,000 structures were calculated in this way. The speed of the potential enables large unit cells, containing up to 64 atoms, to be sampled in this case. The best structures from the EDDP calculations were then used for subsequent DFT calculations using CASTEP⁸⁴. We used the on-the-fly generated ultrasoft, 'QCS' pseudo-potentials, a plane-wave cut off of 440 eV, and k-point spacing of $0.05 \times \frac{2\pi}{\Lambda}$ for searching and training the potentials.

Convex hull. To generate the convex hull of the combined AIRSS and USPEX data, we performed geometry optimizations of all

structures using the same parameters as in the AIRSS searches. All structures within 50 meV of the hull at 0, 2 or 10 GPa were retained for final, well-converged calculations using ‘C19’ pseudopotentials with a plane-wave cut-off of 1000 eV, and k-point spacing of $0.02 \times \frac{2\pi}{A}$.

Electronic and vibrational properties

Electronic and vibrational properties were computed using the QUANTUM ESPRESSO^{85,86} suite, using scalar-relativistic optimized norm-conserving Vanderbilt pseudopotentials (ONCV)^{87,88} and a PBE-GGA parametrization for the exchange and correlation functional⁸⁹. Kohn-Sham orbitals were expanded on plane-waves, with a kinetic energy cutoff of 100 Ry for the wavefunctions and $8 \times 8 \times 8$ unshifted **k**-grid sampling over the BZ⁹⁰ with a Methfessel-Paxton gaussian smearing⁹¹ of 0.04 Ry. Phonon frequencies were obtained by Fourier interpolation of the dynamical matrices on $2 \times 2 \times 2$ **q**-grid within Density Functional Perturbation Theory (DFPT)⁹². Electron-phonon properties were computed on $16 \times 16 \times 16$ **k**-grid. For structures with T_c higher than 10 K, we re-computed the dynamical matrices on a $6 \times 6 \times 6$ **q**-grid and the *el-ph* properties on $30 \times 30 \times 30$ **k**-grid.

Data availability

The data generated in this study have been deposited in the Zenodo database under accession code 7839254⁹³ and in the Supplementary Information file.

Code availability

The codes generated in this study have been deposited in the Zenodo database under accession code 7839254⁹³.

References

- Dasenbrock-Gammon, N. et al. Evidence of near-ambient superconductivity in a N-doped lutetium hydride. *Nature* **615**, 244–250 (2023).
- Lilia, B. et al. The 2021 room-temperature superconductivity roadmap. *J. Phys.: Condens. Matter* **34**, 183002 (2022).
- Drozdov, A. P., Erements, M. I., Troyan, I. A., Ksenofontov, V. & Shylin, S. I. Conventional superconductivity at 203 Kelvin at high pressures in the sulfur hydride system. *Nature* **525**, 73–76 (2015).
- Drozdov, A. P. et al. Superconductivity at 250 K in lanthanum hydride under high pressure. *Nature* **569**, 528–531 (2019).
- Heil, C., Cataldo, S. D., Bachelet, G. B. & Boeri, L. Superconductivity in sodalite-like yttrium hydrides. *Phys. Rev. B* **220502**. <https://doi.org/10.1103/PhysRevB.99.220502> (2019).
- Somayazulu, M. et al. Evidence for superconductivity above 260 K in lanthanum superhydride at megabar pressures. *Phys. Rev. Lett.* **122**, 027001 (2019).
- Sun, Y., Lv, J., Xie, Y., Liu, H. & Ma, Y. Route to a superconducting phase above room temperature in electron-doped hydride compounds under high pressure. *Phys. Rev. Lett.* **123**, 097001 (2019).
- Semenok, D. V. et al. Superconductivity at 161 k in thorium hydride ThH₁₀: synthesis and properties. *Mater. Today* **33**, 36–44 (2020).
- Kong, P. et al. Superconductivity up to 243 K in yttrium hydrides under high pressure. *Nat. Commun.* **12**, 5075 (2021).
- Chen, W. et al. High-temperature superconducting phases in cerium superhydride with a T_c up to 115 K below a pressure of 1 Megabar. *Phys. Rev. Lett.* **127**, 117001 (2021).
- Semenok, D. V. et al. Superconductivity at 253 k in lanthanum-yttrium ternary hydrides. *Mater. Today* **48**, 18–28 (2021).
- Ma, L. et al. High-temperature superconducting phase in clathrate calcium hydride CaH₆ up to 215 k at a pressure of 172 gpa. *Phys. Rev. Lett.* **128**, 167001 (2022).
- Flores-Livas, J. A. et al. A perspective on conventional high-temperature superconductors at high pressure: methods and materials. *Phys. Rep.* **856**, 1–78 (2020).
- Pickard, C. J., Errea, I. & Erements, M. I. Superconducting hydrides under pressure. *Ann. Rev. Condens. Matter Phys.* **11**, 57–76 (2020).
- Hilleke, K. P. & Zurek, E. Rational design of superconducting metal hydrides via chemical pressure tuning. *Angew. Chem. Int. Ed.* **61**, e202207589 (2022).
- Di Cataldo, S., Heil, C., von der Linden, W. & Boeri, L. LaBH₈: towards high- T_c low-pressure superconductivity in ternary superhydrides. *Phys. Rev. B* **104**, L020511 (2021).
- Liang, X. et al. Prediction of high- T_c superconductivity in ternary lanthanum borohydrides. *Phys. Rev. B* **104**, 134501 (2021).
- Lucrezi, R., Di Cataldo, S., von der Linden, W., Boeri, L. & Heil, C. In-silico synthesis of lowest-pressure high- t_c ternary superhydrides. *npj Comput. Materials* **8**. <https://doi.org/10.1038/s41524-022-00801-y> (2022).
- Di Cataldo, S. & Boeri, L. Metal borohydrides as ambient-pressure high- T_c superconductors. *Phys. Rev. B* **107**, L060501 (2023).
- Savini, G., Ferrari, A. C. & Giustino, F. First-principles prediction of doped graphane as a high-temperature electron-phonon superconductor. *Phys. Rev. Lett.* **105**, 037002 (2010).
- Saha, S., Cataldo, S. D., Amsler, M., von der Linden, W. & Boeri, L. High-temperature conventional superconductivity in the boron-carbon system: Material trends. *Phys. Rev. B* **102**, 024519 (2020).
- Cui, X. et al. RbB₃Si₃: an alkali metal borosilicide that is metastable and superconducting at 1 atm. *J. Phys. Chem. C* **124**, 14826–14831 (2020).
- Di Cataldo, S., Qulaghasi, S., Bachelet, G. B. & Boeri, L. High- T_c superconductivity in doped boron-carbon clathrates. *Phys. Rev. B* **105**, 064516 (2022).
- Zhu, L. et al. Superconductivity in SrB₃C₃ clathrate. *Phys. Rev. Res.* **5**, 013012 (2023).
- Ashcroft, N. W. Metallic hydrogen: a high-temperature superconductor? *Phys. Rev. Lett.* **21**, 1748 (1968).
- Ginzburg, V. L. Superfluidity and superconductivity in the universe. *J. Stat. Phys.* **1**, 3–24 (1969).
- Ashcroft, N. W. Hydrogen dominant metallic alloys: high temperature superconductors? *Phys. Rev. Lett.* **92**, 187002 (2004).
- Ming, X. et al. Absence of near-ambient superconductivity in LuH_{2±xNy}. *Nature* 1–3. <https://doi.org/10.1038/s41586-023-06162-w> (2023).
- Shan, P. et al. Pressure-induced color change in the lutetium dihydride LuH₂. *Chin. Phys. Lett.* **40**. <https://iopscience.iop.org/article/10.1088/0256-307X/40/4/046101/meta> (2023).
- Yang Sun, Feng Zhang, Shunqing Wu, Vladimir Antropov & Kai-Ming Ho. Effect of nitrogen doping and pressure on the stability of LuH₃. *Phys. Rev. B* **108**, L020101 (2023).
- Zhao, X. et al. Pressure tuning of optical reflectivity in LuH₂. *Sci. Bull.* **68**, 883–886 (2023).
- Wang, N. et al. Percolation-induced resistivity drop in cold-pressed LuH₂. *arXiv preprint arXiv:2304.00558*. <https://doi.org/10.48550/arXiv.2304.00558> (2023).
- Zhang, YJ., Ming, X., Li, Q. et al. Pressure induced color change and evolution of metallic behavior in nitrogen-doped lutetium hydride. *Sci. China Phys. Mech. Astron.* **66**, 287411 (2023).
- Xing, X. et al. Observation of non-superconducting phase changes in LuH_{2±xNy}. *arXiv preprint arXiv:2303.17587*. <https://doi.org/10.48550/arXiv.2303.17587> (2023).
- Cai, S. et al. No evidence of superconductivity in a compressed sample prepared from lutetium foil and H₂/N₂ gas mixture. *Matter Radiat. Extremes* **8**, 048001 (2023).
- Mingfeng Liu, Xiangyang Liu, Jiangxu Li, Jiayi Liu, Yan Sun, Xing-Qiu Chen & Peitao Liu. Parent structures of near-ambient nitrogen-doped lutetium hydride superconductor. *Phys. Rev. B* **108**, L020102 (2023).

37. Hilleke, K. P. et al. Structure, stability, and superconductivity of N-doped lutetium hydrides at kbar pressures. *Phys. Rev. B* **108**, 014511 (2023).
38. Kim, S.-W., Conway, L. J., Pickard, C. J., Pascut, G. L. & Monserrat, B. Microscopic theory of colour in lutetium hydride. *arXiv:2304.07326* (2023).
39. Pickard, C. J. & Needs, R. J. High-pressure phases of silane. *Phys. Rev. Lett.* **97**, 045504 (2006).
40. Pickard, C. J. & Needs, R. J. Ab initio random structure searching. *J. Phys.: Condens. Matter* **23**, 053201 (2011).
41. Pickard, C. J. Ephemeral data derived potentials for random structure search. *Phys. Rev. B* **106**, 014102 (2022).
42. Glass, C. W., Oganov, A. R. & Hansen, N. Uspex-evolutionary crystal structure prediction. *Comput. Phys. Commun.* **175**, 713–720 (2006).
43. Lyakhov, A. O., Oganov, A. R., Stokes, H. T. & Zhu, Q. New developments in evolutionary structure prediction algorithm USPEX. *Comput. Phys. Commun.* **184**, 1172–1182 (2013).
44. Bonnet, J. E. & Daou, J. N. Rare-earth dihydride compounds: lattice thermal expansion and investigation of the thermal dissociation. *J. Appl. Phys.* **48**, 964–968 (2008).
45. Okamoto, H. et al. Binary alloy phase diagrams. *ASM International, Materials Park, OH, USA* **12** (1990).
46. Hellenbrandt, M. The inorganic crystal structure database (icsd)-present and future. *Crystallogr. Rev.* **10**, 17–22 (2004).
47. Jain, A. et al. Commentary: the materials project: a materials genome approach to accelerating materials innovation. *APL Mater.* **1**. <https://doi.org/10.1063/1.4812323> (2013). 011002.
48. Shao, M. et al. Superconducting ScH₃ and LuH₃ at Megabar Pressures. *Inorg. Chem.* **60**, 15330–15335 (2021).
49. Lucrezi, R., Ferreira, P. P., Aichhorn, M., & Heil, C. Temperature and quantum anharmonic lattice effects in lutetium trihydride: stability and superconductivity. *arXiv preprint arXiv:2304.06685* (2023).
50. Therrien, F., Jones, E. B. & Stevanović, V. Metastable materials discovery in the age of large-scale computation. *Appl. Phys. Rev.* **8**. <https://doi.org/10.1063/5.0049453> (2021). 031310.
51. Yu, S. et al. Pressure-driven formation and stabilization of superconductive chromium hydrides. *Sci. Rep.* **5**. <https://doi.org/10.1038/srep17764> (2015).
52. Errea, I., Calandra, M. & Mauri, F. First-principles theory of anharmonicity and the inverse isotope effect in superconducting palladium-hydride compounds. *Phys. Rev. Lett.* **111**, 177002 (2013).
53. Xie, F. et al. Lu–H–N phase diagram from first-principles calculations. *Chin. Phys. Lett.* **40**, 057401 (2023).
54. Huo, Z. et al. First-principles study on the conventional superconductivity of N-doped fcc-LuH₃. *Matter Radiat. Extremes* **8**, 038402 (2023).
55. Tao, X., Yang, A., Yang, S., Quan, Y. & Zhang, P. Leading components and pressure-induced color changes in N-doped lutetium hydride. *Sci. Bull.* <https://www.sciencedirect.com/science/article/pii/S2095927323003778> (2023).
56. Gubler, M., Krummenacher, M., Finkler, J. A. & Goedecker, S. Ternary phase diagram of nitrogen doped lutetium hydrides. *arXiv preprint arXiv:2306.07746*. <https://doi.org/10.48550/arXiv.2306.07746> (2023).
57. Lonie, D. C. & Zurek, E. Xtalopt: an open-source evolutionary algorithm for crystal structure prediction. *Comput. Phys. Commun.* **182**, 372–387 (2011).
58. Allen, P. B. & Dynes, R. C. Transition temperature of strong-coupled superconductors reanalyzed. *Phys. Rev. B* **12**, 905–922 (1975).
59. Manzeli, S., Ovchinnikov, D., Pasquier, D., Yazyev, O. V. & Kis, A. 2D transition metal dichalcogenides. *Nat. Rev. Mater.* **2**, 1–15 (2017).
60. Choi, H. J., Roundy, D., Sun, H., Cohen, M. L. & Louie, S. G. The origin of the anomalous superconducting properties of MgB₂. *Nature* **418**, 758–760 (2002).
61. Zunger, A. & Freeman, A. J. Band structure and lattice instability of TiSe₂. *Phys. Rev. B* **17**, 1839–1842 (1978).
62. Correa, L. E. et al. Evidence for multiband superconductivity and charge density waves in Ni-doped ZrTe₂. *J. Alloys Compd.* **907**, 164477 (2022).
63. Margine, E. R. & Giustino, F. Anisotropic migdal-eliasberg theory using wannier functions. *Phys. Rev. B* **87**, 024505 (2013).
64. Chen, Y., Zhu, H. & Shanenko, A. A. Interplay of fermi velocities and healing lengths in two-band superconductors. *Phys. Rev. B* **101**, 214510 (2020).
65. Chen, Y. & Shanenko, A. Multiband superconductors: two characteristic lengths for each contributing condensate. *J. Phys. Chem. Lett.* **13**, 10350–10355 (2022).
66. Cercellier, H. et al. Evidence for an excitonic insulator phase in 1T–TiSe₂. *Phys. Rev. Lett.* **99**, 146403 (2007).
67. Zhang, Z. et al. Design principles for high-temperature superconductors with a hydrogen-based alloy backbone at moderate pressure. *Phys. Rev. Lett.* **128**, 047001 (2022).
68. Song, Y. et al. Stoichiometric ternary superhydride LaBeH₈ as a new template for high-temperature superconductivity at 110 K under 80 GPa. *Phys. Rev. Lett.* **130**, 266001 (2023).
69. Vocaturo, R., Tresca, C., Ghiringhelli, G. & Profeta, G. Prediction of ambient-pressure superconductivity in ternary hydride PdCuH_x. *J. Appl. Phys.* **131**, 033903 (2022).
70. Song, H. et al. High T_c superconductivity in heavy rare earth hydrides. *Chin. Phys. Lett.* **38**, 107401 (2021).
71. Duan, D. et al. Pressure-induced metallization of dense (H₂S)₂H₂ with high-T_c superconductivity. *Sci. Rep.* **4**, 6968 (2014).
72. Liang, X. et al. Potential high-T_c superconductivity in CaYH₁₂ under pressure. *Phys. Rev. B* **99**, 100505 (2019).
73. McMahon, J. M. & Ceperley, D. M. High-temperature superconductivity in atomic metallic hydrogen. *Phys. Rev. B* **84**, 144515 (2011).
74. McMillan, W. L. Transition temperature of strong-coupled superconductors. *Phys. Rev.* **167**, 331–344 (1968).
75. Heil, C. & Boeri, L. Influence of bonding on superconductivity in high-pressure hydrides. *Phys. Rev. B* **92**, 060508 (2015).
76. Denchfield, A., Park, H. & Hemley, R. J. Novel electronic structure of nitrogen-doped lutetium hydrides. *arXiv preprint arXiv:2305.18196*. <https://doi.org/10.48550/arXiv.2305.18196> (2023).
77. Pavlov, N. S., Shein, I. R., Pervakov, K. S., Pudalov, V. M. & Nekrasov, I. A. Anatomy of the band structure of the newest apparent near-ambient superconductor LuH_{3-x}N_x. *arXiv preprint arXiv:2306.09868*. <https://doi.org/10.48550/arXiv.2306.09868> (2023).
78. Anisimov, V. I., Zaanen, J. & Andersen, O. K. Band theory and mott insulators: Hubbard U instead of stoner i. *Phys. Rev. B* **44**, 943–954 (1991).
79. Aryasetiawan, F. et al. Frequency-dependent local interactions and low-energy effective models from electronic structure calculations. *Phys. Rev. B* **70**, 195104 (2004).
80. Wu, W., Zeng, Z. & Wang, X. Investigations of pressurized Lu-N-H materials by using the hybrid functional. *arXiv preprint arXiv:2306.11511*. <https://doi.org/10.48550/arXiv.2306.11511> (2023).
81. Sano, W., Koretsune, T., Tadano, T., Akashi, R. & Arita, R. Effect of van hove singularities on high-T_c superconductivity in H₃S. *Phys. Rev. B* **93**, 094525 (2016).
82. Lee, H. et al. Electron-phonon physics from first principles using the EPW code. *arXiv preprint arXiv:2302.08085*. <https://doi.org/10.48550/arXiv.2302.08085> (2023).
83. Kresse, G. & Furthmüller, J. Efficient iterative schemes for ab initio total-energy calculations using a plane-wave basis set. *Phys. Rev. B* **54**, 11169–11186 (1996).
84. Clark, S. J. et al. First principles methods using CASTEP. *Z. für Krist. - Cryst. Mater.* **220**, 567–570 (2005).

85. Giannozzi, P. et al. Advanced capabilities for materials modelling with quantum espresso. *J. Phys.: Condens. Matter* **29**, 465901 (2017).
86. Giannozzi, P. et al. Quantum ESPRESSO toward the exascale. *J. Chem. Phys.* **152**. <https://doi.org/10.1063/5.0005082> (2020). 154105.
87. Hamann, D. R. Optimized norm-conserving vanderbilt pseudopotentials. *Phys. Rev. B* **88**, 085117 (2013).
88. Schlipf, M. & Gygi, F. Optimization algorithm for the generation of oncv pseudopotentials. *Comput. Phys. Commun.* **196**, 36–44 (2015).
89. Perdew, J. P., Burke, K. & Ernzerhof, M. Generalized gradient approximation made simple. *Phys. Rev. Lett.* **77**, 3865–3868 (1996).
90. Monkhorst, H. J. & Pack, J. D. Special points for brillouin-zone integrations. *Phys. Rev. B* **13**, 5188–5192 (1976).
91. Methfessel, M. & Paxton, A. T. High-precision sampling for brillouin-zone integration in metals. *Phys. Rev. B* **40**, 3616–3621 (1989).
92. Baroni, S., de Gironcoli, S., Dal Corso, A. & Giannozzi, P. Phonons and related crystal properties from density-functional perturbation theory. *Rev. Mod. Phys.* **73**, 515–562 (2001).
93. Ferreira, P. P. et al. Search for ambient superconductivity in the Lu-N-H system. <https://doi.org/10.5281/zenodo.7839254> (2023).

Acknowledgements

We would like to acknowledge Roman Lucrezi, Angela Rittsteuer, and Markus Aichhorn for insightful discussions. PPF and LTFE gratefully acknowledge the São Paulo Research Foundation (FAPESP) under Grants 2020/08258-0 and 2021/13441-1. CH acknowledges the Austrian Science Fund (FWF): P 32144-N36. LB acknowledges support from Project PEO00021, "Network 4 Energy Sustainable Transition - NEST", funded by the European Union - NextGenerationEU, under the National Recovery and Resilience Plan (NRRP), Mission 4 Component 2 Investment 1.3 - Call for tender No. 1561 of 11.10.2022 of Ministero dell'Università e della Ricerca (MUR). Calculations were performed on the Vienna Scientific Cluster (proj. 71754 "TEST"), on the dcluster of the Graz University of Technology, on the CINECA cluster (proj. IsC99-ACME-C); Computational resources for the UK partners were provided by the UK's National Supercomputer Service through the UK Car-Parrinello consortium (EP/PO22561/1) and the Cambridge Service for Data Driven Discovery (CSD3) using Tier-2 EPSRC funding (EP/TO22159/1).

Author contributions

P.P.F. and L.J.C. contributed equally. P.P.F., L.J.C., A.C., C.H. and L.B. wrote the main draft. P.P.F. performed the USPEX ternary, pseudo-binaries, and fixed composition searches. E.K. performed the USPEX binary searches. C.J.P. and L.J.C. carried out the AIRSS searches and made the

final relaxation. P.P.F. and A.C. carried out the phonon and *el-ph* calculations. A.C. and L.B. developed the effective superconducting model. L.J.C., S.D.C. and F.G. conducted the HT screening. F.G. performed the XRD pattern assessment and C.H. the Raman analysis. P.P.F., A.C., S.D.C. and L.T.F.E. prepared the figures and tables. C.J.P., C.H. and L.B. supervised this project. All authors participated in the discussions and revised the manuscript.

Competing interests

The authors declare no competing interests.

Additional information

Supplementary information The online version contains supplementary material available at <https://doi.org/10.1038/s41467-023-41005-2>.

Correspondence and requests for materials should be addressed to Chris J. Pickard, Christoph Heil or Lilia Boeri.

Peer review information *Nature Communications* thanks Artem Oganov, Guochun Yang and the other, anonymous, reviewer(s) for their contribution to the peer review of this work. A peer review file is available.

Reprints and permissions information is available at <http://www.nature.com/reprints>

Publisher's note Springer Nature remains neutral with regard to jurisdictional claims in published maps and institutional affiliations.

Open Access This article is licensed under a Creative Commons Attribution 4.0 International License, which permits use, sharing, adaptation, distribution and reproduction in any medium or format, as long as you give appropriate credit to the original author(s) and the source, provide a link to the Creative Commons licence, and indicate if changes were made. The images or other third party material in this article are included in the article's Creative Commons licence, unless indicated otherwise in a credit line to the material. If material is not included in the article's Creative Commons licence and your intended use is not permitted by statutory regulation or exceeds the permitted use, you will need to obtain permission directly from the copyright holder. To view a copy of this licence, visit <http://creativecommons.org/licenses/by/4.0/>.

© The Author(s) 2023